Graphical Abstract

Phase-field simulation of abnormal/normal recrystallization kinetics in ultrafine-grained aluminum processed by high-pressure torsion extrusion

Olena Abramova, Dayan Nugmanov, Daniel Schneider, Andreas Prahs, Tobias Mittnacht, Julia Ivanisenko, Brigitte Baretzky, Britta Nestler

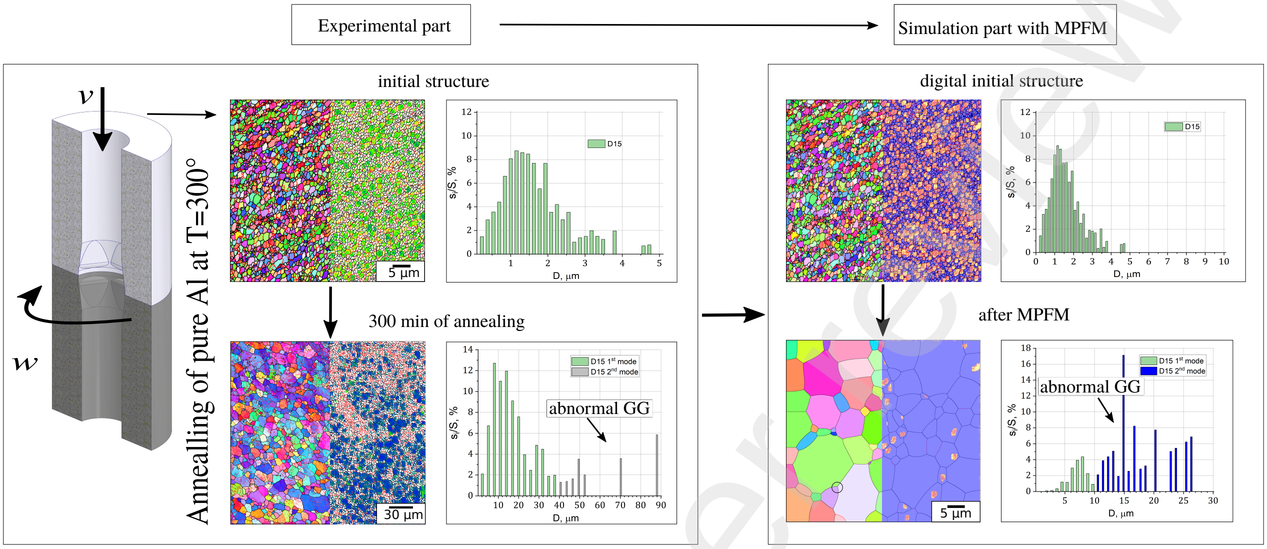

Highlights

Phase-field simulation of abnormal/normal recrystallization kinetics in ultrafine-grained aluminum processed by high-pressure torsion extrusion

Olena Abramova, Dayan Nugmanov, Daniel Schneider, Andreas Prahs, Tobias Mittnacht, Julia Ivanisenko, Brigitte Baretzky, Britta Nestler

- The abnormal grain growth was simulated by a multiphase field model.
- The digital twin of the recrystallization process in the structure of severely plastically deformed pure aluminum allowed to investigate the nature of the initialization of abnormal grain growth.
- The main reason for the initialization of abnormal grain growth was the heterogeneous distribution of dislocation density in the initially deformed aluminum.

Phase-field simulation of abnormal/normal recrystallization kinetics in ultrafine-grained aluminum processed by high-pressure torsion extrusion

Olena Abramova[a,*], Dayan Nugmanov[a], Daniel Schneider[a,c], Andreas Prahs[b], Tobias Mittnacht[b], Julia Ivanisenko[a], Brigitte Baretzky[a] and Britta Nestler[a,b,c]

[a] *Institute of Nanotechnology (INT), Karlsruhe Institute of Technology (KIT), Hermann-von-Helmholtz-Platz 1, Eggenstein-Leopoldshafen, 76344, Germany*

[b] *Institute for Applied Materials - Microstructure Modelling and Simulation (IAM-MMS), Karlsruhe Institute of Technology (KIT), Strasse am Forum 7, Karlsruhe, 76131, Germany*

[c] *Institute of Digital Materials (IDM), Karlsruhe University of Applied Sciences, Moltkestrasse 30, Karlsruhe, 76133, Germany*

ARTICLE INFO

Keywords:
Recrystallization
Grain growth simulation
Phase-field model

ABSTRACT

The digital twin of the recrystallization (ReX) kinetics in pure Al subjected to severe plastic deformation by high-pressure torsion extrusion (HPTE) was created, using the multiphase-field model (MPFM). After the HPTE, an experimental study of the ReX kinetics of pure Al at 300°C was carried out. The deformed structure of Al was implemented for the ReX simulation by the MPFM. The simulated ReX kinetics show that the bimodal distributions of (sub)grain size are formed, which are consistent with the experiment. Furthermore, the MPFM calculation proposes a transition of the ReX kinetics from normal to abnormal grain growth (NGG and AGG), without a separation of grains into fractions with different grain growth rates. The analysis of the simulated microstructures makes it possible to determine the criteria for the development of NGG and AGG.

List of abbreviations

AGG - abnormal grain growth;
CS - calculated steps;
D2 - size of the grains with both LAGB and HAGB;
D15 - size of the grains with HAGB;
EBSD - electron backscatter diffraction;
ECAE - equal channel angle extrusion;
FEM - finite element method;
GND - geometrically necessary dislocations;
HAGB - high-angle grain boundary ($\Theta > 15°$);
LAGB - low-angle grain boundary ($2° < \Theta < 15°$);
NGG - normal grain growth;
OIM - orientation imaging microscopy;
PACE3D - Parallel Algorithms for Crystal Evolution in 3D;
MPFM - multiphase-field model;
RD - radial direction;
s_i/S - specific area fraction of the corresponding crystallite size intervals;
SD - shear direction;
SE - stored energy;
SEA - stored energy areas;
SEM - scanning electron microscope;
SFE - stacking fault energy;
SPD - severe plastic deformation;
UFG - ultra-fine grains;
V_{HAGBs} - volume fraction of high-angle grain boundaries;
Θ - misorientation angle.

1. Introduction

Despite many years of studying recrystallization (ReX) kinetics, this problem is still a subject of research in materials undergoing severe plastic deformation (SPD). Control of ReX kinetics is a way to stabilize the morphology undergoing grain refinement and improve the performance and technological properties of ultrafine grained materials, which occur as a result of recovery and ReX. Comprehending the principles underlying ReX necessitates the identification of governing parameters that induce and restrain coarsening through regulation of grain boundary migration.Small-scale grain boundary migration provides normal grain growth, which is described by an Arrhenius-type equation [1]:

$$D^2 - D_0^2 = 2\alpha\gamma M \cdot t = \kappa t, \tag{1}$$

with D as the mean grain diameter, the initial mean grain diameter D_0 at time $t = 0$, a geometric constant α, the grain boundary energy γ, and the grain boundary mobility M. The introduced parameter $k = 2\alpha\gamma M$ is used to quantify the evolution of the mean grain size.

In general, models describing grain growth in polycrystal microstructures suggest that excess grain boundary energy manifests itself in the form of interfacial energy, which is a driving force for boundary migration along the mean curvature of the boundary [2, 3, 4]. Assuming equal or nearly equal interfacial energy for all grain boundaries, the mean grain diameter increases correspondingly at low temperature (Eq. 1), which is confirmed by both theory [4, 5] and computer simulations [6, 7, 8].

As captured in Eq. (1), grain boundary mobility is a controlling factor determining the microstructure after ReX.

---

[*] Corresponding author
olena.abramova@kit.edu (Olena Abramova)
ORCID(s):

For annealed Al at temperatures below 400K [9], Winning et al. [9] demonstrated theoretically that the mobility M for low-angle grain boundaries (LAGBs) is lower than that of high-angle grain boundaries (HAGBs). On the contrary, a higher annealing temperature of 900 K provides a higher mobility of subgrains, which can result in various ReX mechanisms at different temperatures [9]. This finding is in good agreement with the experimental observation that the LAGB network exhibits higher stability than the HAGB network, during annealing after deformation at temperatures below 573 K, both after conventional deformation [10, 11] and after SPD by accumulated roll bonding [12], equal channel angle extrusion (ECAE) [13], and high- pressure torsion [14].

In pure materials, grain growth can be highly anisotropic, with a small subpopulation of grains growing rapidly to sizes more than an order of magnitude larger than the rest of the population. It is hypothesized that rapidly growing grains benefit from an energy and/or mobility advantage that allows their boundaries to move rapidly through a matrix of quasi-anchored neighboring grains. This mode of growth corresponds to the standard definition of abnormal grain growth (AGG) [15]. Although AGG has been under investigation for over 50 years, it remains subject of current research [3, 16, 17]. AGG is not uncommon at micron grain sizes in coarse grain materials, and AGG may be even more common in ultrafine grains (UFG) than in originally coarse-grained materials [18]. Based on the observation of Braun et al [18], it can be assumed that an extended period of 'normal' ReX of UFG materials may contribute to the appearance of new AGG modes.

In general, most modeling methods assume that ReX evolves via the formation and growth of nuclei. However, in cases where the formation of ReX nuclei is not required due to the presence of ultrafine grains with predominantly high angular boundaries, it becomes important to consider the migration kinetics of existing LAGBs and HAGBs, as well as the change in misorientation angles of these boundaries during annealing. Creating a digital twin of a real structure formed during ReX enables the exploration of extensive datasets and facilitates the prognostication of reciprocal interactions among structural factors [19]. Since the ReX processes in severely deformed materials with high stacking fault energy (SFE) are not well understood, we design a digital twin to simulate the annealing of the aluminum microstructure, taking into account the recovery and static recrystallization processes using the multiphase-field model (MPFM). The MPFM is expected to provide new insights into the change of normal/abnormal ReX kinetics during the annealing of an aluminum polycrystalline material.

In the present work, the recrystallization kinetics of pure UFG aluminum produced by HPTE at room temperature is being investigated experimentally and through simulation. Taking into account the complexity of the subject under investigation and the variety of processes occurring during ReX, this work focuses on the driving forces that facilitate the movement of boundaries. These driving forces aim to minimize the free energy accumulated during previous deformation and reduce the interfacial energy. The interfacial energy, in turn, is determined by both the curved shape of these boundaries and their total length. Additionally, the mobility of the boundaries is largely determined by their misorientation.

2. Materials and Methods

2.1. Used material and specimens

Material Commercially pure aluminum rod samples containing 99.5 Al, 0.3–0.4 Si, less than 0.1–0.2 Fe, Mg, Co and other impurities (all wt. %, AA1050, supplied by MaTeck Material Technologie & Kristalle GmbH) were machined, extruded from 20.0 to 11.8 mm diameter and annealed at 345°C for 30 min, with final water cooling to room temperature. The thermal treatment was performed to reduce residual stresses and achieve a homogeneous microstructure. Cylindrical aluminum samples with a length of 35 mm were processed at room temperature using a computer-controlled HPTE machine (manufacturer: W. Klement GmbH, Lang, Austria). Molybdenum disulfide (MoS_2) was used as a lubricant in all experiments to facilitate the extrusion process. The HPTE equipment used in this study has been described in detail in [20], using an advanced hexagonal shape of HPTE dies [21].

Specimen The samples were individually extruded through the die, using a punch moving at an extrusion speed v and a lower die rotating at a rotational speed ω. As a result, the specimens underwent both expansion-extrusion deformation and torsional deformation in a narrow zone where both dies meet. The billets were annealed at 300°C and subsequently quenched in water. The duration of the annealing process was varied from 10 min to 5 hours. The microstructure evolution of HPTE treated specimens was investigated at the transverse cross section located at the center of the billet height during annealing.

2.2. Image generation and processing

Generation of EBSD images Microstructure investigations were performed using a scanning electron microscope: Zeiss LEO and Zeiss Auriga 60 (SEM), operating at 20 kV. The Zeiss Auriga 60 scanning electron microscope with electron backscatter diffraction (EBSD) detector was used to analyze grain morphology and grain boundary misorientations. To prepare the samples for analysis, they were initially sectioned perpendicular to the extrusion axis, then grinded and mechanically polished. Finally, at room temperature, discs with a diameter of 3 mm and a thickness of ~150 µm electropolished using the A3 electrolyte by Struers. Electropolishing was performed at a voltage of 20 V and a current of 10 A.

Processing of EBSD images The EBSD images were evaluated using the orientation imaging (OIM) software by EDAX. The scanning step size ranged from 25 nm to 1 µm, which corresponds to the size of one pixel. The

Table 1

Microstructure parameters obtained from OIM: the grain size D15, the subgrain size D2, the volume fraction of HAGBs V_{HAGBs}, the density of HAGBs, the average misorientation angle of the full map Θ, the average misorientation angle in the fraction of the 2^{nd}-mode grains $\Theta_{2^{nd}mode}$, the density of GNDs, and the ratio N_{SD}/N_{RD}

Process ID	D15 [a], μm	D2, μm	$V_{2^{nd}mode}/V$, %	V_{HAGBs}, %	L_{HAGBs}/S	Θ,°	$\Theta_{2^{nd}mode}$,°	GND, $\times 10^{12}$m^{-2}	N_{SD}/N_{RD}
deformed	1.3	1.2	0	78.4	2.62	32.8	–	172.5	1.23
10 min	1.6	1.3	0	90.1	2.34	37.8	–	115.9	1.08
30 min	2.3–6.0	2.1	10.8	91.5	1.59	38.0	12.2	38.1	0.88
60 min	6.7–27.3	4.7	15.9	72.4	0.613	32.9	10.3	21.7	0.79
300 min	15.8–67.4	10.7	21.2	54.7	0.289	25.4	7.7	12.1	1.01

---

[a] the two values separated by a dash correspond to the values of the first and second maximum in the size distribution D

EBSD study was performed on the transversal section of the HPTE-processed specimens near the edge, specifically at approximately ∼4.0 mm from the central axis of the rod. The horizontal direction of the rectangular scan plane was parallel to the outer radial direction (RD), the vertical direction was parallel to the shear direction (SD) (see Fig. 1). To ensure the reliability of the EBSD data, a cleaning process was performed using the grain dilation cleanup and neighbor orientation correlation options of the OIM software. All grains consisting of four pixels or less were automatically removed from the EBSD maps. A lower limit boundary misorientation threshold of 2° was applied to eliminate disputable orientations caused by orientation noise. To distinguish between low-angle grain boundaries (LAGBs) and high-angle grain boundaries (HAGBs) a threshold value of 15° is consider, here similar to [15]. For the characterization of the average statistical data of the structure, the volume fraction of HAGB (V_{HAGBs}) was determined as the fraction of misorientations larger than 15°, in the total set of misorientations. Grain size was calculated using the equal diameter method [22]. Accordingly, the mean diameter of a circle whose surface area is equal to the surface area of crystallite bounded by the boundaries with misorientations of 2° and higher is named subgrain size (D2), while the mean diameter of a circle whose surface area is equal to the surface area of crystallite bounded by the boundaries with misorientations of 15° and higher is denoted as grain size (D15). The histograms of the grain and subgrain size distributions were plotted for the specific area fraction (s_i/S) of the corresponding crystallite size intervals. The characterization of grain elongation was determined by calculating the ratio of the number of intersections of lines drawn along the SD and RD with grain boundaries, represented by N_{SD} and N_{RD}, respectively. The density of HAGB is estimated by the ratio L_{HAGBs}/S, where L_{HAGBs} is the length of the HAGBs within the scan area S. To account for the EBSD detector resolution, the critical angle of 2° was considered as the lowest value of subgrain misorientation that could be measured. Misorientations smaller than 2° were considered as integral misorientations, which occur as a consequence of the local curvature of the crystal lattice, due to geometrically necessary dislocations (GND). The GND density values were calculated using TSL OIM EDAX v.7 software (EDAX Inc., Draper, UT, USA). The software employed default settings for fcc (face-centered cubic) crystal-type slip systems. The calculation of GND density, specifically considered slip in (111) crystallographic planes and four possible slip systems along four close-packed <110> directions. The GND density was determined using the GND map reconstruction option. For additional information regarding the GND density calculation can be found in a separate reference [23].

3. Experimental results

3.1. Orientation imaging, mean grain size and grain boundary misorientations

OIM maps of the HPTE-processed aluminum before (a) and after annealing (b-d) are shown in Fig. 1. The initial structure shown in Fig. 1 a) is used as the input for the ReX simulation studies. It is well-established that the microstructures formed after SPD contain a significant number of LAGBs. As a result, almost all grains are bounded by both high- and low-angle grain boundaries. This can also be observed in the structure of HPTE-deformed aluminum (Fig. 1 a). Since the mobility of low-angle grain boundaries is much lower than the mobility of high-angle grain boundaries, the analysis of the kinetics of recrystallization and grain growth in such materials has a number of peculiarities.

To analyze the changes in grain size during annealing, a characteristic grain size needs to be determined. For conventionally deformed materials, it is common to use the size of crystallites limited only by HAGBs with misorientations greater than or equal to 15° (D15) as such a size. However, for materials deformed at low homologous temperatures and with a significant fraction of LAGBs, it is also beneficial to examine the change in D2 size. The experimentally reconstructed inverse pole images (left parts in Fig. 1) and the maps of the GND distribution (right parts of the microstructures in Fig. 1) are considered for the purpose of comparing the simulations and experimental results in terms of statistically determined quantitative characteristics. In the deformed state (Fig. 1 a), of the aluminum specimen exhibits slightly elongated grains with an aspect ratio (N_{SD}/N_{RD} = 1.23), a normal grain size distribution, and average grain sizes of D2 = 1.2 μm and D15 = 1.5 μm (Fig. 1 a). In both the deformed and 30 minutes

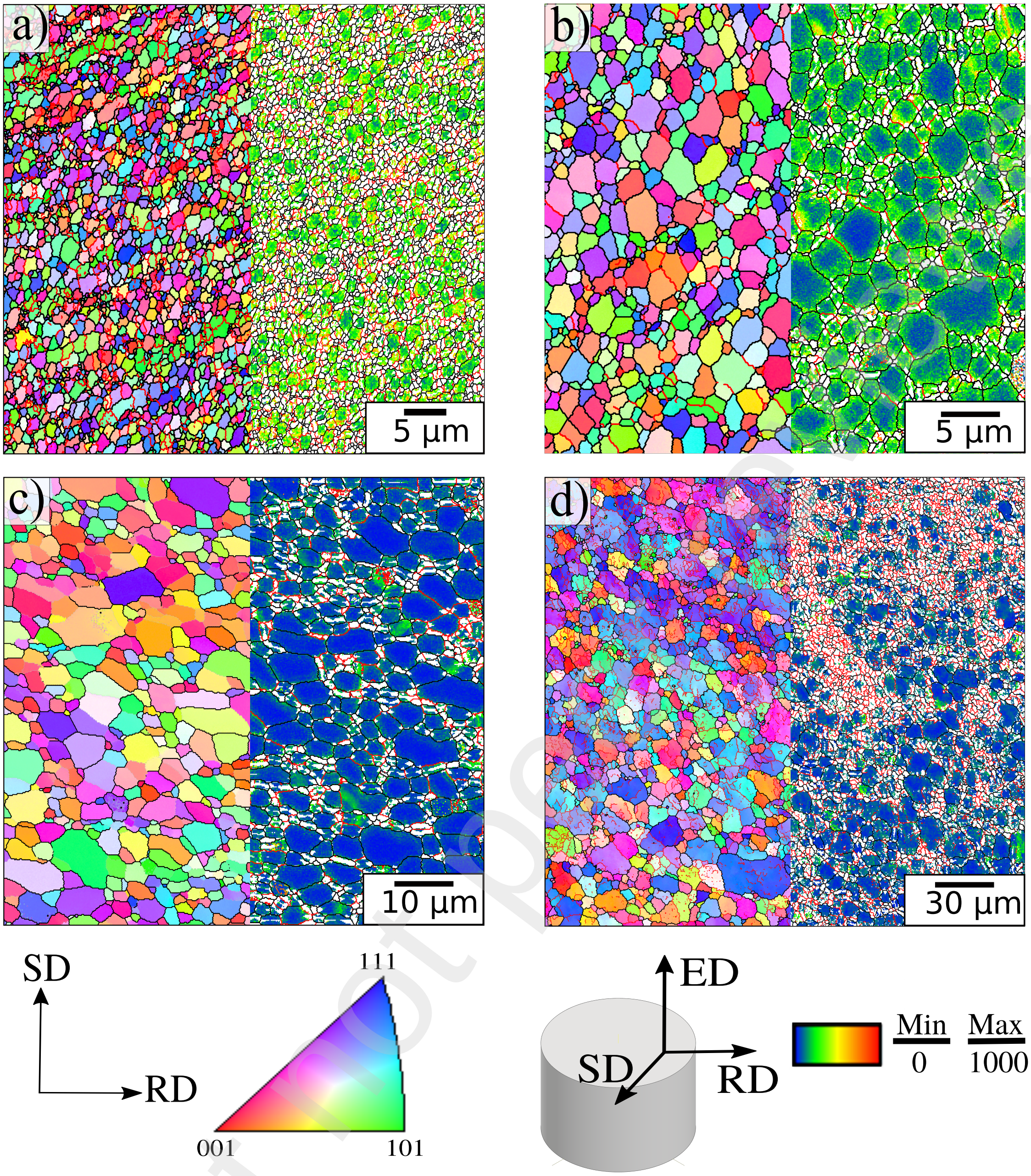

Figure 1: Microstructure of the HPTE-processed Al in deformed state (a) and after annealing at 300°C, during 30 min (b), 60 min (c), and 300 min (d). Inverse pole figure maps (left) show typical areas of aluminum structures. Geometrically necessary dislocation density distributions (right) is shown in a color-coded map at the scale [$\times 10^{12}$m^{-2}]. The outer directions, the standard stereographic triangle, and the GND density scale are shown in the lower part of the figure. HAGBs are indicated by the black lines, LAGBs by the red lines.

of annealed microstructures, the D2 grains are located within larger D15 grains and have at least one high-angle (HA) boundary (Fig. 1 a, b). Annealing for 10 and 30 minutes results in the formation of equiaxed grains, indicated by a decreased N_{SD}/N_{RD} ratio as shown in Table 1. The 60-minute annealing was accompanied by a gradual increase in the grain sizes D2 and D15, with the size of D15 growing faster than D2, as observed in Fig. 1 b, c. In the structure after 60 and 300 minutes of annealing, it is clearly visible that each large grain contains many LAGBs (Fig. 1 c, d).

These large grains evolve a spherical shape, reducing the aspect ratio N_{SD}/N_{RD} from 1.23 to 0.79, after 60 minutes of annealing (Table 1).

An important feature of the structure after annealings for 30 and 60 minutes is the presence of large grains with low GND density (grains with a size of D15 = 10 µm or more in Fig. 1 b, c). Areas with increased GND density are

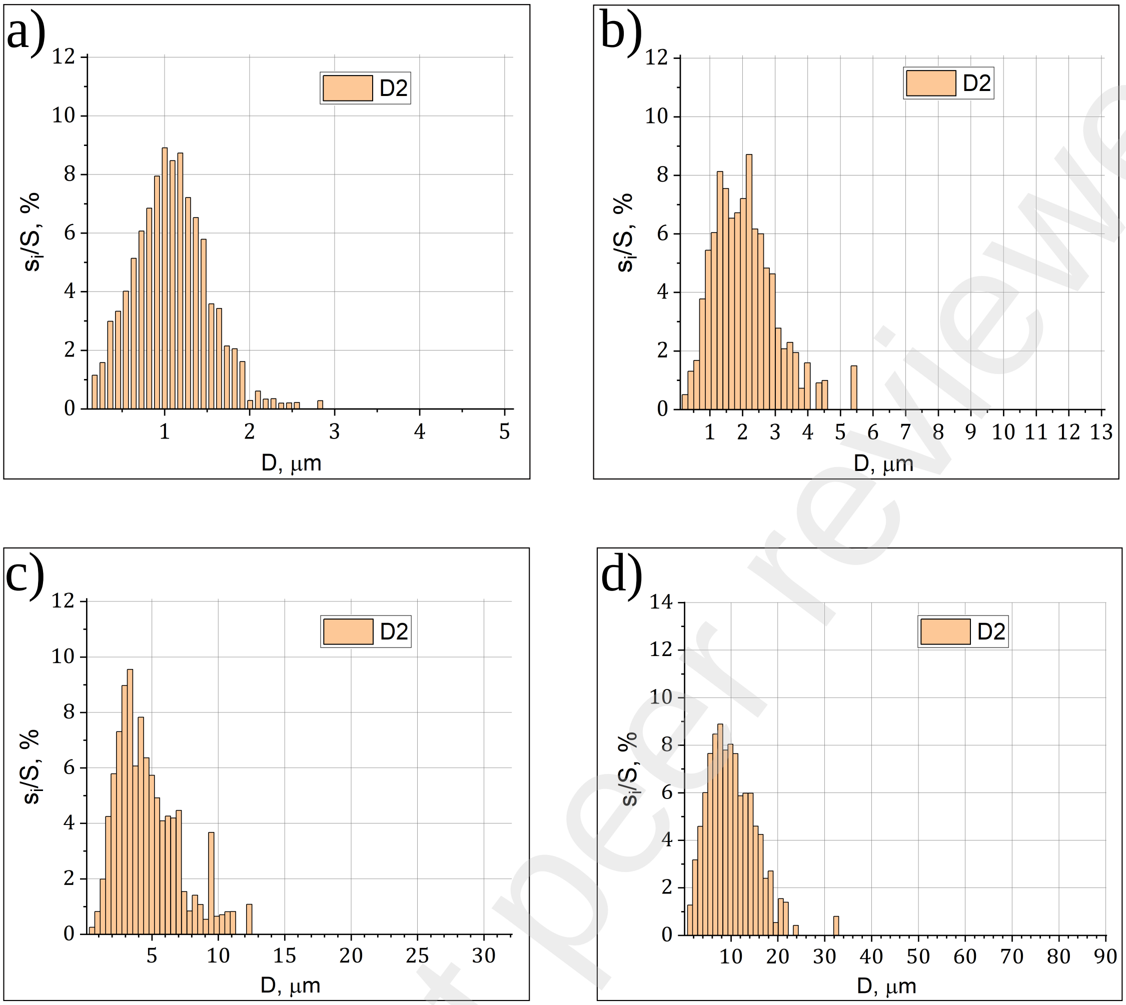

Figure 2: Distribution of D2 with respect to the specific area s_i/S of HPTE-processed Al (a) in the deformed state and (b) after annealing at 300°C for 30 minutes, (c) 60 minutes, and (d) 300 minutes.

characterized in these states by small grains of 1–2 μm in size. After 300 minutes of annealing (Fig. 1 d), the average GND density is already so low that it is complicated to establish any correlation between grain size and GND density. It is important to note that in the initial state, a majority of the grain boundaries were curved, which is considered as evidence of the boundaries being in a non-equilibrium state according to the literature [24]. The curved shape can be observed after 30 and 60 minutes of annealing, but not after 300 minutes of annealing (Fig. 1 b-d). Additionally, after 300 minutes, a large majority of the grain boundary triple junctions in the structure exhibit approximately equal angles close to 120° (Fig. 1 d). Such a configuration of triple junctions, as well as the absence of curved grain boundaries, is characterized in the literature as equilibrium [15].

The density of HAGBs, estimated by L/S, decreases during recrystallization (as documented in Table 1 and subsequently illustrated by Fig. 8 b). Compared to the decrease of the GND density with increasing annealing time, the change of the HAGBs-density is smoothly, almost linearly, up to an annealing time of 60 minutes . Subsequent annealing between 60 and 300 minutes resulted in a more gradual decrease in HAGB density.

3.2. Geometrically necessary dislocations

Effect of annealing on GND density. In Fig. 1, the images on the right show the distributions of GND density values on the same maps as those on the left of Fig. 1, which represent orientation distribution maps. In the initially deformed structure in each grain, the GND density has a minimum value in the center of the grain and increases towards the grain boundary (Fig. 1 a). Exactly at the boundary, the GND density is zero, which is an artifact related to the measurement method [15].

Annealing for 30 minutes resulted in a sharp decrease in the average GND density from $172\times10^{12}\text{m}^{-2}$ in the deformed state to $38.1\times10^{12}\text{m}^{-2}$ (Table 1). A further decrease of the GND density can be observed after 60 minutes and 300 minutes of annealing (Table 1). Most important for the development of ReX is the decrease in the average GND

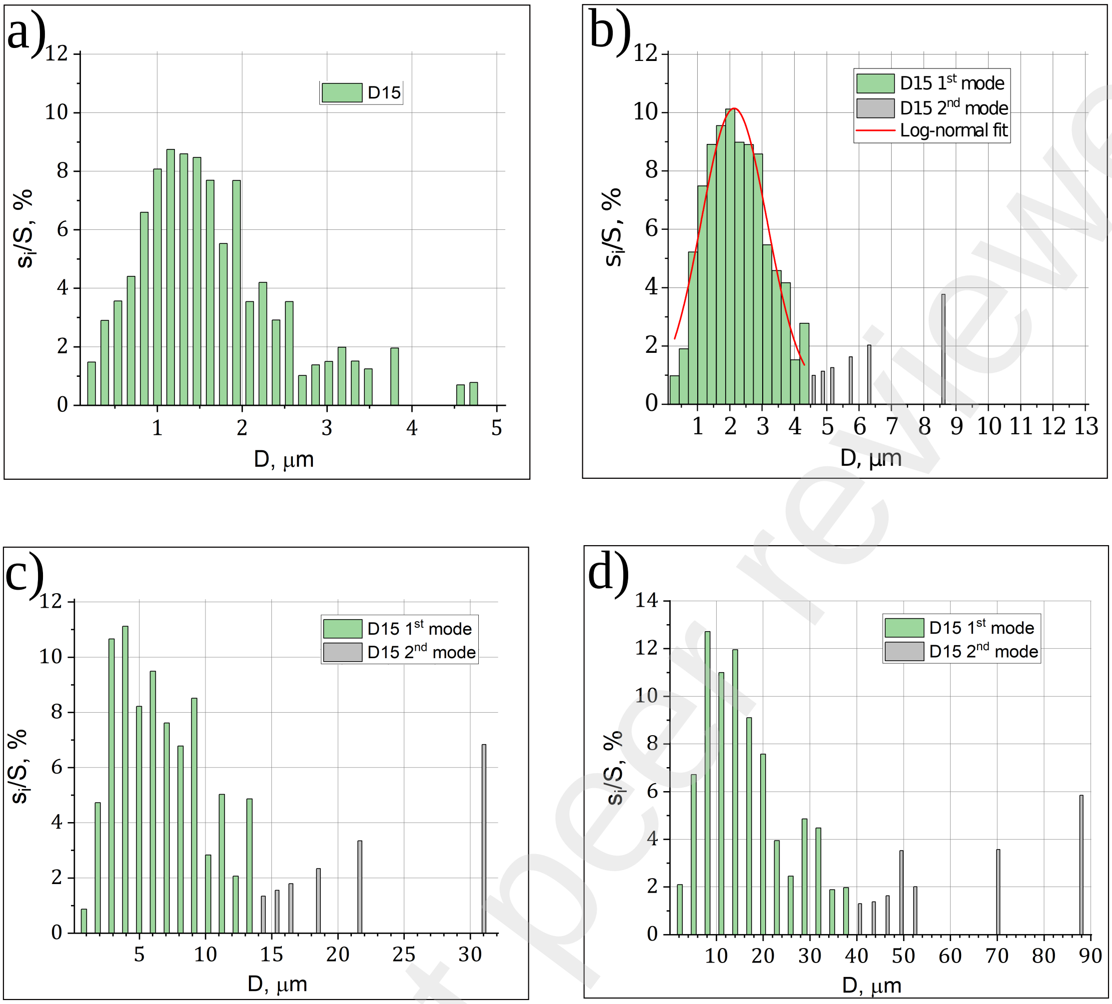

Figure 3: Distribution of the D15 parameter with respect to the specific area s_i/S of HPTE-processed Al (a) in the deformed state and (b) after annealing at 300°C for 30 minutes, (c) 60 minutes and (d) 300 minutes.

density and the disappearance of the GND density gradient for neighboring grains, which is due to the low GND density in both grains.

According to the GND density maps (1 b and c), the GND density in the grain centers shows a decrease after annealing for 30 and 60 minutes, respectively. Even after annealing, the GNDs were heterogeneously distributed across the grains: For some grains, the density decreased to a minimum after 300 minutes of annealing, while for other grains, it remained the same as in the deformed state (cf. Fig. 1 b and c). Thus, an annealing time of 30 minutes resulted in the disappearance of fine grains, a significant decrease in the GND density, and the onset of abnormal grain growth.

3.3. Analysis of the grain size distributions

The separation of the 1st and 2nd modes in histograms due to AGG is methodologically involved, since there are insufficient statistics on large grains. Regarding D15, the position of the maximum of the second peak, for example, cannot be determined in the structure of metals and alloys, due to partial recrystallization during hot deformation [25], and, consequently, the non-existent gap between the two distributions of mode one and two. Approximating the first peak by a Gaussian distribution allows the width of the distribution and the limit of the first mode to be determined, as illustrated in Fig. 3 b).

The experimentally obtained size distribution histograms D2 are presented in Fig. 2. The distribution histograms D2 of the initial samples (Fig. 2 a) and of the samples after an annealing time of 30 up to 300 minutes (Fig. 2 b-d) have the form of a lognormal distribution. As the duration of the annealing increases, the maximum of the distribution shifts towards larger values of D2 from ∼2 microns after 30 minutes of annealing (Fig. 2 b) to ∼10 microns after 300 minutes of annealing (Fig. 2 d).

Experimental histograms of the D15 distribution of the deformed state have the form of a lognormal distribution with one mode and a maximum at 1.2 microns (Fig. 3 a). After 30 minutes of annealing, the second mode begins to form in the histogram, and the peak of the first mode shifts to 2.0 µm (Fig. 3 b). The approximation of the first mode of the D15 distribution by a lognormal function is shown in Fig. 3 b) by the red line. Using this approximation, it is possible to unambiguously divide the histogram into two modes. For a detailed analysis in TSL OIM, the second mode is marked as a separate fraction in gray (Fig. 3 b-d). After annealings for 60 and 300 minutes, the second mode in the D15 distribution is shifted to the region of large grains, like the first mode (Fig. 3 c-d). The formation of the second mode in the histogram of the D15 distribution clearly indicates the development of the AGG process, which begins after only 30 min of annealing HPTE-deformed aluminum.

The difference between D2 and D15 did not exceed the standard deviation for an annealing time up to 30 minutes (Table 1). After 30 minutes of annealing, a pronounced bimodality formed in the D15 size distribution, making the average grain size a less meaningful indicator. The structure with the bimodal D15 size distribution is characterized by distribution maxima corresponding to 2.3 and 6.0 µm after 30 minutes of annealing (Table 1). The grain size D2 and the first and second maximum D15 after 60 minutes of annealing were 4.7, 6.7, and 27.3 µm , respectively, and reached 10.7, 15.8, and 67.4 µm after 300 minutes (Table 1).

Thus, pure aluminum subjected to HPTE exhibits very typical recrystallization kinetics for SPD materials. The primary NGG stage is clearly present, accompanied by a significant drop in dislocation density (Table 1). In addition, the recrystallization kinetics has a second phase where the dislocation density is already close to the well-annealed state of aluminum (Table 1). Similarly, the grain size distribution becomes bimodal, which indicates anomalous grain growth (Fig. 3).

4. Phase-field modeling

4.1. Free energy functional

Functional and interfacial contributions A multicomponent multiphase-field model presented by Nestler et al. [19], which includes the consideration of the interfacial energy variation according to Read-Shockley [26, 27] and the interfacial mobility variation according to Humphreys [28], is used to simulate the ReX process. To account for the stored energy in the system, which acts as a bulk driving force for ReX and reduces the deformation-induced dislocations in a system, an additional bulk energy term is included following the approach of Vondrous et al. [26, 29]. Thus, the free energy functional reads as

$$\begin{aligned}\mathcal{F} &= \int_V f\,\mathrm{d}V = \int_V \left(W_{\mathrm{intf}} + \overline{W}_{\mathrm{bulk}}\right)\mathrm{d}V,\\ W_{\mathrm{intf}} &= \varepsilon a(\boldsymbol{\phi},\boldsymbol{\nabla\phi}) + \frac{1}{\varepsilon}\omega(\boldsymbol{\phi}), \quad \overline{W}_{\mathrm{bulk}} = f_{\mathrm{RX}}(\boldsymbol{\phi},\rho_d),\end{aligned} \tag{2}$$

where W_{intf} denotes the interfacial and $\overline{W}_{\mathrm{bulk}}$ is the bulk contribution of the free energy density. The N-tuple of continuous order parameters is referred to as $\boldsymbol{\phi} = \{\phi_1, \dots, \phi_\alpha, \dots, \phi_N\}$, where each order parameter, $\phi_\alpha(\boldsymbol{x}, t)$, represents the volume fraction of a particular phase α /grain α. The interfacial energy density consists of the gradient contribution $\varepsilon a(\boldsymbol{\phi},\boldsymbol{\nabla\phi})$ and the multi-obstacle type potential $\omega(\boldsymbol{\phi})/\varepsilon$. The thickness of the diffuse interface is proportional to the parameter ε. According to Nestler et al. [19], the gradient energy density is defined as

$$\varepsilon a(\boldsymbol{\phi},\boldsymbol{\nabla\phi}) = \varepsilon \sum_{\alpha<\beta} \gamma_{\alpha\beta} |\phi_\alpha \boldsymbol{\nabla}\phi_\beta - \phi_\beta \boldsymbol{\nabla}\phi_\alpha|^2, \tag{3}$$

where $\gamma_{\alpha\beta}$ denotes the interfacial energy between the phases/grains α and β. A detailed description regarding the multi-obstacle potential $\omega(\boldsymbol{\phi})$ is given, e.g., by [19, 30].

Bulk contribution The bulk energy density term $\overline{W}_{\mathrm{bulk}}$, which depends on the dislocation density ρ_d, represents the stored energy of the system and is defined as

$$\overline{W}_{\mathrm{bulk}}(\boldsymbol{\phi},\rho_d) = W_{\mathrm{bulk}}(\rho_d) \sum_{\alpha}^{N} m_\alpha h(\phi_\alpha), \tag{4}$$

$$W_{\mathrm{bulk}}(\rho_d) = \frac{1}{2}\rho_d G b^2, \tag{5}$$

where G is the shear modulus and b is the Burgers vector [27]. In the present work, $h(\phi_\alpha) = \phi_\alpha$ is used as interpolation function. The phase-inherent storage parameter m_α is related to the conventional theory of the static ReX. It indicates whether a phase recrystallizes or not, in the sense that $m_\alpha = 0$ refers to phase with zero bulk energy, while $m_\alpha = 1$ indicates a non-zero bulk energy phase. Once a cell is fully recrystallized, the stored energy becomes zero. Consequently, $\overline{W}_{\mathrm{bulk}}$ decreases as a recrystallizing phase/grain grows.

4.2. Evolution equation

Taking into account the constraint $\sum_\alpha \phi_\alpha = 1$, the evolution equation according to the variational approach of Steinbach and Pezzolla [31] is:

$$\frac{\partial \phi_\alpha}{\partial t} = -\frac{1}{\epsilon \tilde{N}} \sum_{\beta\neq\alpha}^{\tilde{N}} M_{\alpha\beta}(\Theta) \left[\frac{\delta f}{\delta \phi_\alpha} - \frac{\delta f}{\delta \phi_\beta}\right], \quad \forall \phi_\alpha, \alpha = 0, ..., \tilde{N}, \tag{6}$$

where $\tilde{N}$ denotes the number of locally active phases. In this context, the variational derivative is used, which reads as follows:

$$\frac{\delta f}{\delta \phi_\alpha} = \frac{\partial f}{\partial \phi_\alpha} - \mathrm{div}\left[\frac{\partial f}{\partial \boldsymbol{\nabla}\phi_\alpha}\right], \tag{7}$$

where $\boldsymbol{\nabla}\phi_\alpha$ is the gradient of the order parameter ϕ_α and $\mathrm{div}(\cdot)$ represents the divergence operator. The volumetric energy densities in interfacial regions can be evaluated such that the deviation from the equilibrium profile is minimized [32]. Then, the evolution equation reads

$$\frac{\partial \phi_\alpha}{\partial t} = -\frac{1}{\epsilon \tilde{N}} \sum_{\beta\neq\alpha}^{\tilde{N}} M_{\alpha\beta} \left[\frac{\delta W^{\mathrm{intf}}}{\delta \phi_\alpha} - \frac{\delta W^{\mathrm{intf}}}{\delta \phi_\beta} + \frac{8\sqrt{\phi_\alpha \phi_\beta}}{\pi} \Delta W^{\alpha\beta}_{\mathrm{bulk}}\right].$$

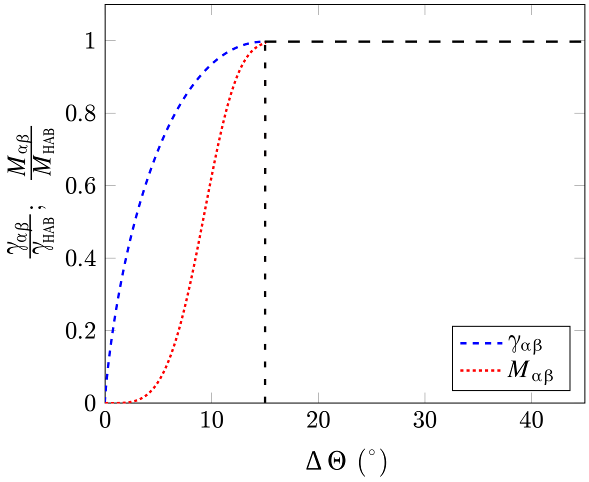

Figure 4: Surface energy and mobility as a function of misorientation of crystal lattices (Eqs. 9 and 10) between two grains for γ_{HAGB}=1 J/m^2 and M_{HAGB}=1 m^4(Js)$^{-1}$. Above a misorientation of $\Delta\Theta_{\mathrm{m}} = 15°$, the value is constant.

(8)

with $\Delta W^{\alpha\beta}_{\mathrm{bulk}} = \dfrac{\partial \overline{W}_{\mathrm{bulk}}}{\partial \phi_\alpha} - \dfrac{\partial \overline{W}_{\mathrm{bulk}}}{\partial \phi_\beta}$, cf., e.g., [32, 33].

The ReX simulation of a two-dimensional computational domain contains up to $N = 10000$ grains. Correspondingly, the evolution of N phases is calculated by N evolution equations of the form as in Eq. 8. To properly account for the reduction in memory requirements, a method for reducing local order parameters is incorporated [34].

Considered parameters In the work at hand, the interfacial energy $\gamma_{\alpha\beta}$ is a function of the misorientation angle $\Delta\Theta_{\alpha\beta}$ between the grains α and β, which is in accordance with Read and Shockley [27] and reads

$$\gamma_{\alpha\beta}(\Delta\Theta_{\alpha\beta}) = \begin{cases} \gamma_{\mathrm{HAGB}} \dfrac{\Delta\Theta_{\alpha\beta}}{\Delta\Theta_m}\left(1 - \ln\dfrac{\Delta\Theta_{\alpha\beta}}{\Delta\Theta_m}\right), & \Delta\Theta_{\alpha\beta} < \Delta\Theta_m \\ \gamma_{\mathrm{HAGB}}, & \text{else.} \end{cases} \tag{9}$$

In this context, γ_{HAGB} is the interfacial energy of a HAGB. The transition from a LAGB to a HAGB takes place at $\Delta\Theta_m = 15°$. Consequently, according to Humphreys [28], the mobility between the phases α and β can be written as

$$M_{\alpha\beta}(\Delta\Theta_{\alpha\beta}) = \begin{cases} M_{\mathrm{HAGB}} \left[1 - \exp\left(-5\left(\dfrac{\Delta\Theta_{\alpha\beta}}{\Delta\Theta_{\mathrm{m}}}\right)^4\right)\right], & \text{else} \\ M_{\mathrm{HAGB}}, & \text{for } \Delta\Theta_{\alpha\beta} > \Delta\Theta_{\mathrm{m}}, \end{cases} \tag{10}$$

where M_{HAGB} models the mobility of a HAGB. In particular, for small misorientations, both the mobility and the interfacial energy density nearly vanish, as shown in Fig. 4.

In the present work, the Read-Shockley model is used for simulation by extending it to all kinds of grain boundaries such as [110] tilt or twist grain boundaries, which is a significant simplification. Furthermore, the energy is assumed to remain constant for a misorientation angle which exceeds the introduced threshold value Θ_{max}, cf., e.g., Vondrous et al. [35].

5. Simulation results

5.1. Grain structure

In the present work, simulation studies are performed with the multiphase and multiphysics framework PACE3D [34]. The microstructures resulting from the simulation of the recrystallization process are visualized in Fig. 5 a-d. The changes in the shape and orientation of the grains are analyzed using the distribution maps of the orientations of the modeled structures, displayed on the left side of the structures in Fig. 5. On the right side of the modeled structures in Fig. 5, the distribution of the stored energy (SE) in the structure is depicted.

The simulated parameters are analysed on a non-dimensional time scale based on the number of simulation time multiplied by the calculation step value (CS = calculation step ×100). The orientation image map in the left column of Fig. 5 a) illustrate the orientation of the grains of the initial structure imported from experimental data (Fig. 1 a). Moreover, the right column of Fig. 5 a) illustrates the regions with initially high GND density by the areas that are not colored in blue. Regarding Fig. 5 a), the red lines highlight the LAGBs while HAGBs are represented by black lines. The areas of stored energy (SEA) in these maps correspond to the size and shape of the high GND regions within the grains, as shown on the GND map in Fig. 5 a. Furthermore, the simulated structures shown in Fig. 5 b-d, exhibit grain boundaries resembling the shape of grain boundaries found in experimental structures with varying annealing durations. In the initially deformed aluminum (Fig. 1 a), most of the grain boundaries exhibit a curved shape, indicating their nonequilibrium state [15]. As the grains grow, the triple junctions at the boundaries, which are not in equilibrium, disappear (Fig. 5 a, b). Based on the misorientations, most of the boundaries, both before and after grain growth, are identified as HAGB (indicated by black lines in Fig. 5).

During the relaxation of the structure, significant grain growth is observed after only 400 CS (Fig. 5 b). This leads to the formation of larger equiaxed grains. Note, the size and distribution of the SEA significantly change compared to the imported initial structure (Fig. 5 a). The amount of SEA, represented by N_{SEA} resulting of minimisation of the W_{bulk}. The remaining SEA retain their previous intensity and shape. During the first 300 CSs the average value of the SE decreases continuously, cf. Table 2. Then, after 300 CS, the relaxation process noticeably accelerates, as indicated in Table 2 (after 400 CS $N_{SEA} = 181$).

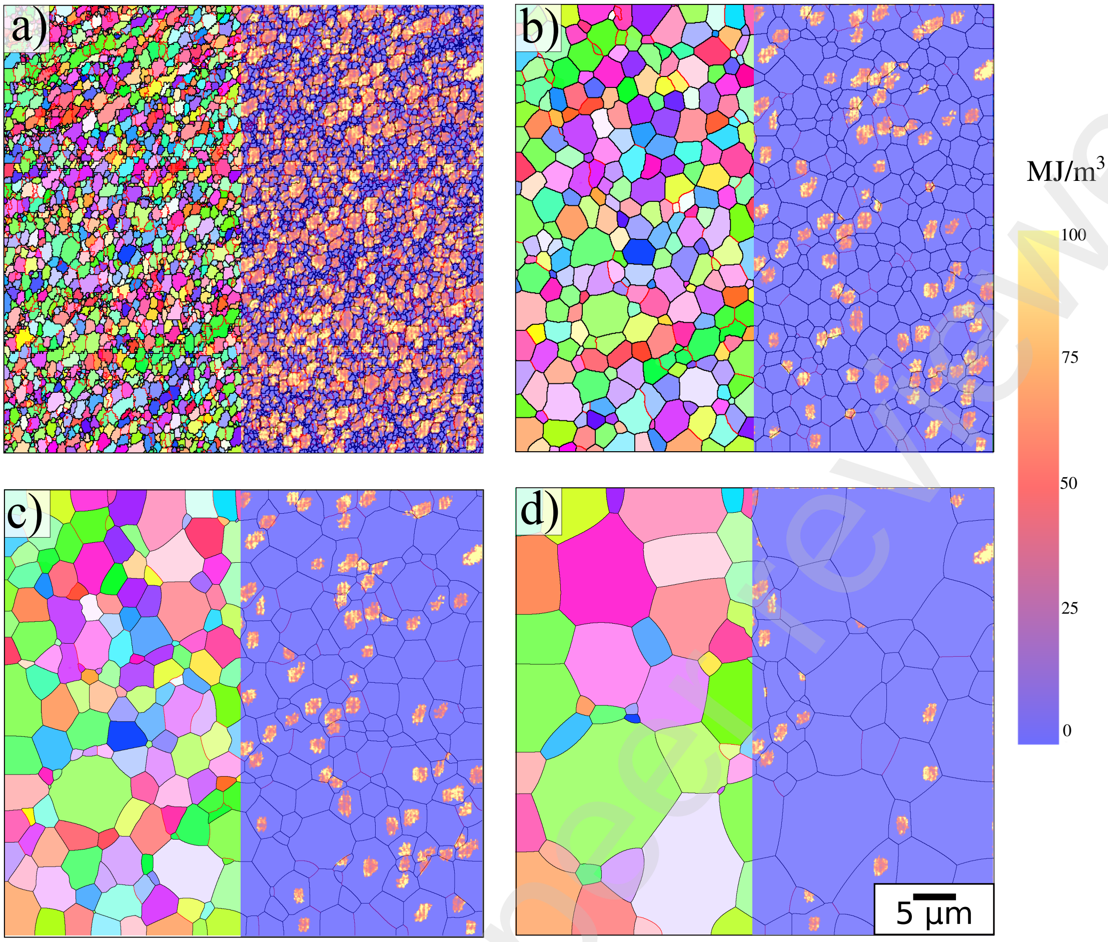

Figure 5: Oriented image maps of the simulated structures of HPTE-processed Al (left) imported initial structure (a), after 400 (b) 564 (c), 1212 (d) CS of PACE3D calculation. The stored energy distribution is shown on the right side of (a-d). On the left, the orientations of the grains are marked using the standard stereographic triangular angles (the orientations are shown in Fig. 1).

Table 2
Microstructure parameters simulated with PACE3D.

CS	D2 [a], µm	D15, µm	$V_{2^{nd}mode}/V$, %	Θ_{sim},°	V_{HAGBs}, %	SE, MJ/m^3	N_{SEA}	$\Theta_{2^{nd}mode}$,°
1	1.2	1.3	–	33.5	80.5	23.51	310	-
9	1.2	1.8	–	33.7	79.7	23.51	192	-
200	3.1	4.4	–	35.0	82.7	23.35	192	-
300	3.4	4.3–10.6	8.1	35.2	82.9	23.23	192	-
400	5.0–8.0	5.7–10.4	16.1	36.5	86.2	20.78	181	10.7
564	5.6–9.4	6.6–12.7	40.1	37.1	93.2	15.40	133	22.1
812	6.8–13.9	7.1–14.6	62.7	40.4	95.5	9.28	90	26.6
1212	6.8–18.8	7.0–19.2	83.6	40.3	98.4	2.95	28	39.2

---

[a] D2 and D15 – The mean grain size values are given for states with lognormal distributions, and the peak size values of D2 and D15 are given for states with bimodal distributions.

The simulated structures in the initial state of ReX are characterized by lognormally distributed histograms of D2 and D15 values up to 400 CS (Fig. 6, Fig. 7). Therefore, the average grain sizes D15 and D2 characterize the simulated structure in the initial state of ReX up to 300 CS, respectively (Table 2).

5.2. D2 size distribution histograms for the simulated structures

The simulated structures are characterized by a lognormal D2 size distribution up to 564 CS (Fig. 6 a-c). With an increase in the number of CS up to 564 (Fig. 6 a-c), the distribution of D2 shifts to the region of large values.

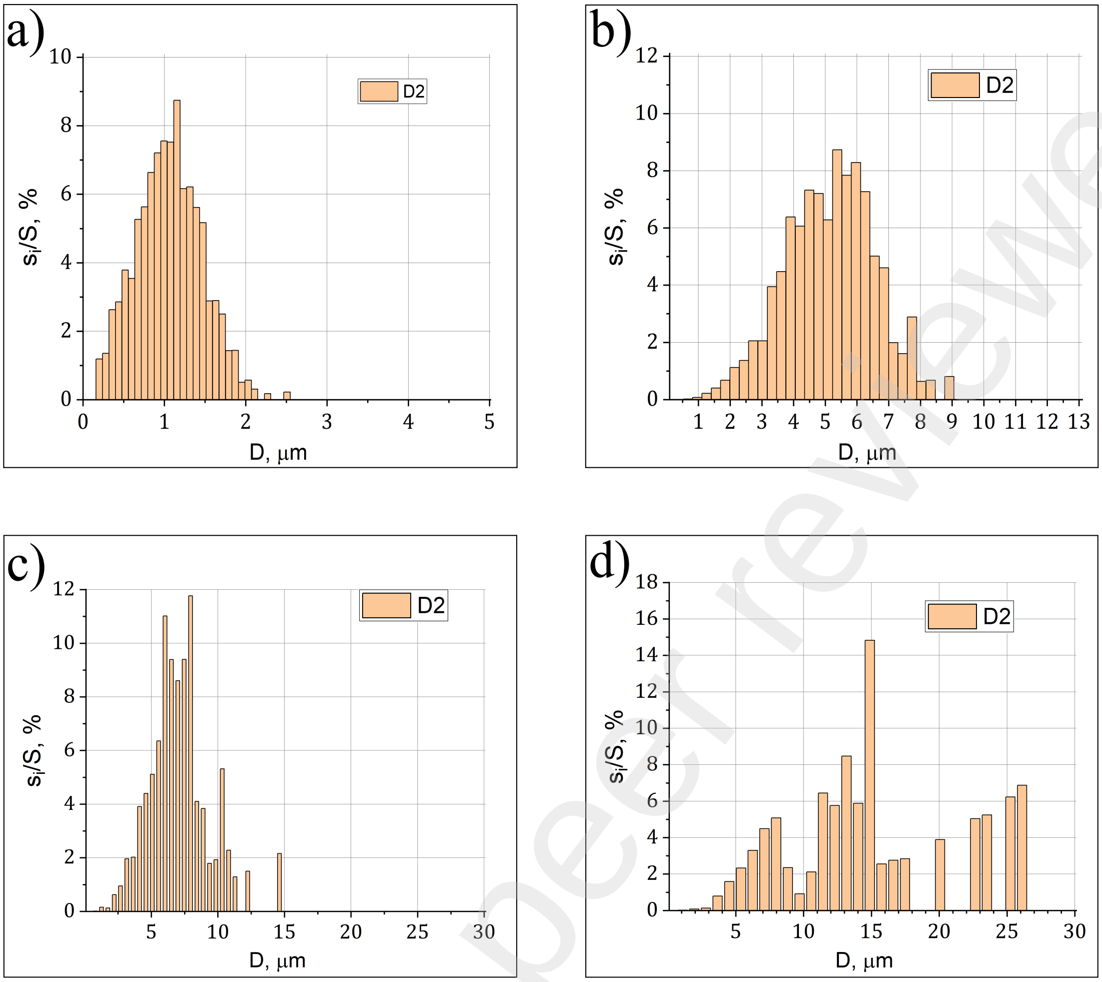

Figure 6: Grain size distributions D2 by specific area s_i/S of HPTE-processed Al after PACE3D imported initial structure (a), after 400 (b), 564 (c) and 1212 (d) CS

The initial stage of recrystallization can be determined from the lognormal histograms of the D2 size distribution of the imported initial structure (a) and after 400 CS, cf. Fig. 6 a, b. Thus, the recrystallization kinetics can be characterized as normal, up to 400 CS [15].

At the 564 CS, large grains appear in the 14–16 μm range (Fig. 5 c). After 1212 CS, the proportion of low-angle grain boundaries in the simulated structure drops to 1.6%. Therefore, almost all grains are surrounded by HAGB. For this state, the change of D2 is negligible.

5.3. D15 size distribution histograms for the simulated structures.

As illustrated by Fig. 7, a lognormal distribution of D15 is obtained up to the first 400 CS. This recrystallization kinetics up to 400 CS can be characterized as normal. With an increase in the number of CS up to 564 (Fig. 7 a-d), the D15 distribution shifts into the region of large D values, still indicating normal grain growth. At computation step 400, the first large grains appear in the 12–13 μm region (Fig. 7 b). The size of 12–13 micrometers becomes the maximum of the second peak in the distribution (Fig. 7 c). Thus, the beginning of AGG is between 400 and 564 CS.

After 1212 CS, determining the position of the maximum of the second mode on the D15 distribution is involved due to the insufficient statistics. However, an increase in the volume fraction and grain sizes is observed, which form the second mode in the D15 distribution (Fig. 7 c, d), indicating the further development of AGG.

In the histograms of the distribution of D15 values, the subsequent modeling shows a different kinetics of the change in the maximum size of D15 in the first and second modes (Fig. 7 c, d). After 812 CS (Table 2), the average D15 size of the first mode reaches a saturation value of ∼ 7 μm. After 1212 CS (Fig. 7d), the average D15 size of the second mode increased from an initial ∼ 10 to 19.2 μm. Considering the dependence of the average grain size D2 and D15 in the second mode on the number of calculated steps, there is a good agreement with the normal criteria for grain growth, according to the Arrhenius equation (Eq. 1).

After 812 CS (Fig. 8 a), conversely, the average size of the simulated D2 and D15 values in the first mode changes

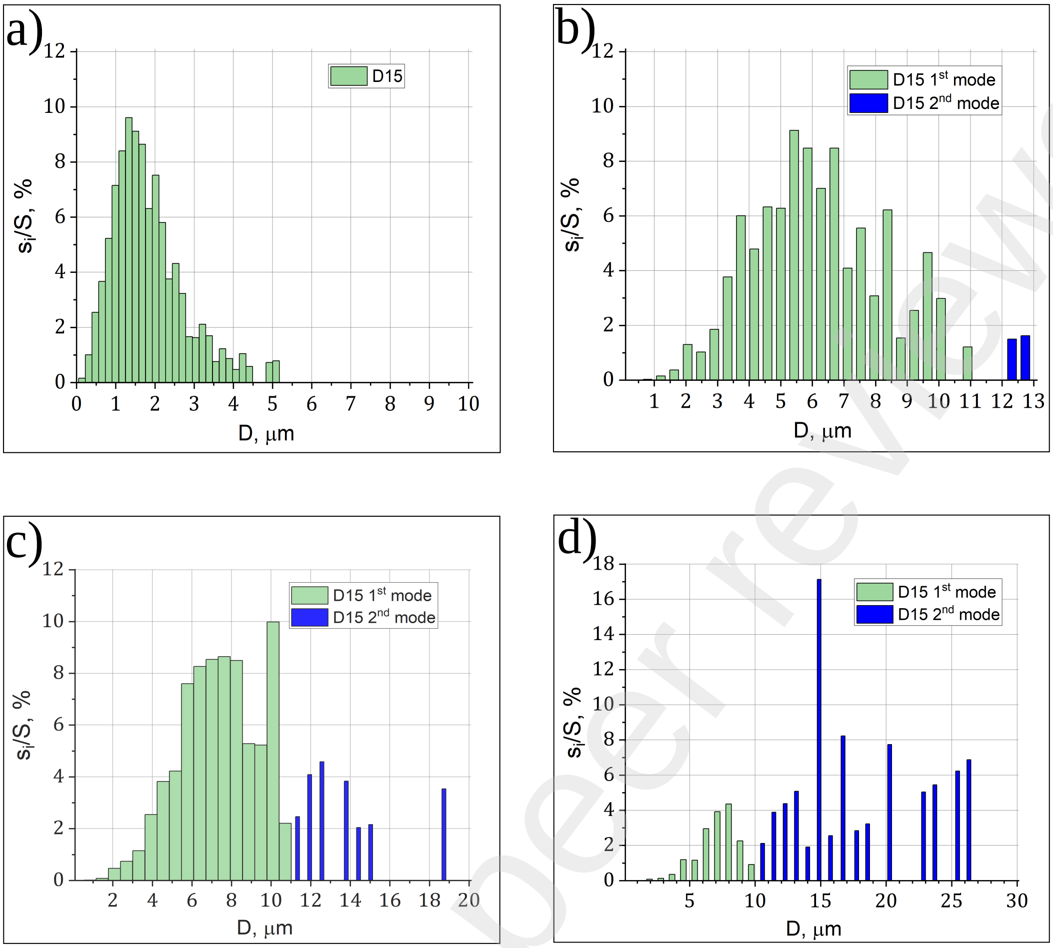

Figure 7: Grain size distributions D15 by specific area si/S of HPTE-processed Al after PACE3D imported initial structure (a), after 400 (b), 564 (c) and 1212 (d) CS .

similarly to the saturation near 7 µm. Large grains that form a new mode are marked with blue bars in the D15 histogram (Fig. 7 c-d). The average grain sizes D15 and D2 for the simulated structures are shown in Fig. 8 a) separately from the sizes of the first mode. Grain growth in the first mode reaches saturation of the calculated values D2 and D15 after 500 CS (Fig. 8 a). In contrast of the saturation stages of the D2 and D15 for the first mode, obtained by the simulation, the dependence of the experimental values of the first mode of the D2 and D15 distribution does not exhibit a saturation stage (Fig. 2 b-d, Fig. 3 b-d). The experimentally observed dependence of D2 and D15 exhibit a slow increase in the interval between one and five hours of annealing.

5.4. Misorientation angles

The misorientation angle Θ_{sim} of the simulated structures mainly increases within the first 812 CS from 33.7° to ~40°, cf. Table 2. The subsequent change up to 1212 CS is negligible small. Moreover, the average misorientation of the grain boundaries, which form the second mode in the histogram of the D15 size distribution, also increases with an increasing number of CS ($\Theta_{2^{nd} mode}$ in Table 2). The value of the misorientation angle of the second mode is slightly smaller than that of the first mode.

Note the discrepancy between the experimental and model values for the ratio of HAGB to LAGB after 30 minutes of annealing and 564 CS, respectively. The experimentally observed decrease in volume fraction V_{HAGB}, from 91.5% after 30 minutes of annealing to 54.7% after 300 minutes of annealing (Table 1), is not observed in the simulated structures, where V_{HAGB} only increases with increasing CS (Table 2).

6. Discussion

6.1. Normal grain growth

In the simulated kinetics of ReX, the stage of normal grain growth observed correlates with the experimental NGG stage, characterized by an increased dislocation density and a gradual decrease in SE levels (Fig. 8 b). The values of the dislocation density determines the bulk contribution W_{bulk} of the free energy and, consequently, impacts the bulk driving force. Since $\gamma_{\alpha\beta}$ depends on the misorientation angle, the interfacial free energy W_{intf}, cf.

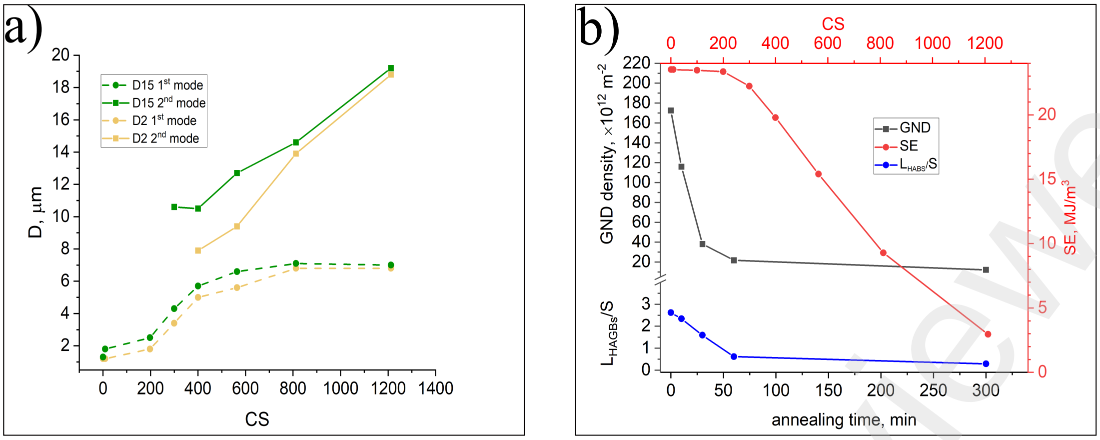

Figure 8: Evolution of the microstructure parameters during recrystallization of HPTE-processed Al, during annealing at 300°C: calculated grain size D15 and D2 depending on the CS (a), experimental GND density and specific length of the HAGB depending on the annealing time and calculated average SE depending on the CS (b).

Eq. 3, and, thus, the interfacial driving force is affected by the grain boundaries density. The decrease in GND density to the level of well-annealed aluminum after 60 minutes of annealing (Table 1), leads to a reduction in W_{bulk} contribution to the total energy and a decrease in the average SE value (Fig. 8 b). This decrease in GND density is accompanied by the initiation of AGG. A possible interpretation is that elevated GND and SE levels are a necessary prerequisite for NGG, and their decline triggers the onset of AGG.

Considering the correlation between GND value and average grain misorientation observed after the first 30 minutes of annealing (Table 1), it can be assumed that GND density is the main factor controlling NGG. In the simulated structures, the main factor is the SEA density, which correlates with Θ_{sim}. In the considered modeling of ReX and the development of AGG, the value of $\Theta_{2^{nd} mode}$ increases from 10.7°, after 400 CS, to 39.2°, after 1212 CS, when the specific grain volume of the second mode in the grain size distribution reaches 83.6% (Table 2).

In previously published studies on modeling the recrystallization process using MPFM for pure aluminum, the transition from NGG to AGG was not observed [36, 37]. The calculation of W_{bulk}, considering the distribution of dislocation density, was implemented in works modeling MPFM recrystallization on steel [26] and aluminum [38]. However, in both of these works only NGG was observed, such as within the first 400 CS in the current study. It is worth noting that in the mentioned works [38, 26], the initial grain structure was a Voronoi tessellation, in which a high dislocation density was not specified. As a result, the contribution of W_{bulk} to the total energy of the system (Table 1) remained constant and relatively insignificant throughout the recrystallization process, compared to other components of the total energy in [26, 38].

6.2. Abnormal grain growth

As the annealing time exceeds 30 minutes and the number of CS over 400, a second mode is observed in the histograms of the grain size distribution (Fig. 2 a, b and Fig. 6 d), indicating the development of AGG. The presence of AGG is particularly pronounced in the grain size distribution of D15.

In Fig. 8 b, the rates of decrease in the average GND and SE values during the recrystallization process are shown. The SE parameter is computed taking into account both the GND distribution and the GB configuration (Table 1). However, in the UFG structure, the contribution of surface energy at the grain boundaries becomes more significant. The MPFM simulation demonstrates that even at 400 CS, a noticeable heterogeneity in the distribution of SEA emerges in the aluminum structure. This heterogeneity is accompanied by the appearance of a second mode in the grain size distributions (D2 and D15) (Fig. 6 b, Fig. 7 b).

The simulated structures clearly indicate that the newly formed abnormally growing grains do not contain the SEA (Fig. 5 c, d). This observation aligns with the experimental OIM maps, where abnormally growing grains exhibit low GND densities (Fig. 1 c, d). Based on the correlation between the presence of SEA and the occurrence of AGG, it can be concluded that the main cause of AGG is the heterogeneous relaxation rate of stored energy within the structure.

The mechanism of heterogeneous grain growth in the MPFM was demonstrated in [39]. It was shown that due to the different mobility of grain boundaries under the influence of an anisotropic elastic field, the initially equiaxed grains exhibit a non-equilibrium shape, characterized by curved boundaries and non-120° triple junctions. In the presence of a non-uniform distribution of SEA, the field of driving forces for ReX also becomes anisotropic. In this study, the 'stabilization' of small grains in areas with a higher density of SEA leads to their slow growth. Conversely, in areas with significantly smaller SEA value, growing grains tend to adopt a more equiaxed shape with equilibrium triple junctions of boundaries (Fig. 5 c, d).

The discrepancy between the experimental observations and the model regarding the change in the proportion of HAGBs during recrystallization, suggests that the difference in the mobility of LAGBs and HAGBs (Fig. 4) is more significant than accounted for by the Read-Shockley model considered for the computations. Experimental observations have shown that the mobility of grain boundaries at 300°C is highly dependent on the misorientation [40, 41]. However, the assumed curve $M = f(\Theta)$ for the dependence of grain boundary energy on the misorientation (Fig. 4) generally provides a correct estimate, except for grain boundaries with coherent interphase, which exhibit a significantly small interfacial energy.

A similar distribution of boundary mobility with saturation was used, for example, in modeling the recrystallization of pure aluminum (MPFM) in [36]. Based on the constraint obtained in that study, the mobility of grain boundaries in pure aluminum increases sharply for misorientations of 5° and higher. The simulated structures obtained on the basis of such a distribution of boundary mobility show an increase in the proportion of low-angle grain boundaries, with an increase in the nominal exposure time [36]. According to the simulation results in [36], exceptionally normal grain growth is observed, and the graphs of the dependence of the average grain size on the nominal holding time in logarithmic coordinates show linear dependences.

It is important to note that the initial structure modeled in [36] did not contain an increased dislocation density and normal grain growth occurred only because of the minimization of surface energy in the structure.

The authors of [36] pointed out an exponential dependence of the average grain size on the conditional holding time, which aligns with the dependence of the second mode maximum on the number of CS. However, this exponential dependence is not consistent with the dependence of the first mode maximum (which stabilizes after 400 CS) on the D15 distribution observed in the work at hand (Fig. 7). Note, overall, the discrepancy between the ratio of HAGB and LAGB in the experiment and in the simulation does not affect the formation of the bimodal distribution of D15 and AGG as a whole.

The applied model of recrystallization in PACE3D offers the capability to combine the recrystallization that develops in the highly deformed initial structure with the growth of grains, due to the minimization of the area of their boundaries. The applied two-dimensional model provides the qualitative simulation of the kinetics of abnormal grain growth of UFG aluminum. The model accounts for a successive change in the driving force of recrystallization, transitioning from a decrease in dislocation density to the minimization of surface energy. This approach enables the generation of bimodal grain size distributions without artificially segregating grains into fractions with different grain boundary mobilities, as implemented in the work on modeling strontium titanate AGG [42]. Considering various recrystallization mechanisms, the developed digital model provides a more accurate representation of the complex process of recrystallization in aluminum structures, bringing it closer to the experimentally observed process. This integrated approach enhances the understanding and simulation of the recrystallization phenomena in UFG aluminum, improving the reliability and applicability of the model for practical applications.

7. Conclusions

By combining experimental observations with computational modeling, the presented investigations elucidate the fundamental mechanisms underlying the recrystallization and grain growth behavior of SPD-processed aluminum. Regarding the initiation of the abnormal grain growth in deformed pure *fcc* metals it is shown that the heterogeneous distribution of the dislocation density yields the appearance of the crystals with low dislocation density during the grain growth. The grains with low dislocation density are the abnormally growing grains. The number of these grains and their area fraction increase with the processing time.

The simulations based on the MPFM and carried out in the in-home software suite PACE3D allow for predicting the kinetics of recrystallization, as well as the transition from normal to abnormal grain growth.

Acknowledgement

The authors gratefully acknowledge financial support of the research through the programmes “Virtual Materials Design” VirtMat project no.P05 and “Material Systems Engineering (MSE)” of the Helmholtz association. Data and data processing are provided within the KNMFi and MDMC initiatives (no. 43.31.01) through the research data infrastructure KADI4MAT `https://kadi.iam.kit.edu`.

A. Creation of a digital twin from EBSD data

Data conversion. Regarding the overall workflow, a so-called digital twin is used with respect to the measured EBSD data. For this purpose, the experimentally obtained EBSD data is first converted into a format that is compatible with a regular finite difference grid, compatible with the internally used software suite PACE3D (Parallel Algorithms for Crystal Evolution in 3D). In this context, the following work packages are implemented:

- Each grid point is represented by a line vector containing information about the position, the three Euler angles, and the calculation of the stored energy, which is saved in a text file for data transmission.
- To build a grain structure, the Euler angles, which take into account the crystal orientation of each grid point, are mapped to all discretization points of the finite difference grid.
- The data obtained by EBSD measurements are not yet sufficiently resolved to perform reliable phase-field simulations. To overcome this obstacle, a grid

refinement step is performed so that a grain has a diameter of at least 10–12 grid points, which allows the simulation framework to appropriately handle the large number of phases even with a diffuse interface approach [26].

- Apart from the Euler angles, the stored energy information is assigned to the respective grid point in a separate spatially dependent scalar field.

Another assumption is that above a high-angle grain boundary threshold Θ_{max}, the energy remains constant [35]. The saturation level in the simulations reached by the M parameter is the upper boundary.

Since this work is mainly concerned with continuous recrystallization processes in aluminum, classical nucleation theory, as known from various solid-state transformation processes in other alloy systems, will not provide a reliable basis for the phase-field simulations [43, 44]. This is the case, because recrystallization occurs due to low driving forces caused exclusively by stored energy, due to deformation, in contrast to high driving forces that occur, for example, in solidification processes or solid-state precipitation. Apart from that, the differences in interfacial energies, according to the aforementioned Read-Shockley relation, are very high and thus favor the high-angle grain boundary migration. Furthermore, it seems unlikely that thermal fluctuations themselves could form defect-free regions within a high-angle grain boundary network. Hence, it is likely that the nuclei that form new recrystallized grains do not emerge during the annealing process, but are already present in the deformed state before annealing sets in. In fact, there are three well-known recrystallization nucleation models in literature [16]. Beck and Sperry [45] identify the migration of pre-existing HAGB into the interior of neighboring highly strained grains as a main mechanism. The Cahn-Cottrell [46] model, based on the models of Beck [47] and Cahn [48], considers grains and low-angle grain boundaries surrounding regions of low dislocation density. A formed or pre-existing subgrain can grow at the expense of neighboring grains by thermally assisted subgrain boundary migration, resulting in a reduction of stored energy, due to the elimination and rearrangement of microstructural defects. Sandström et al. [49] as well as Varma and Willits [50] and Blum et al. [51] observed that the behavior of subgrain growth in pure aluminum, at elevated temperatures from 300 to 400°C, matches the conditions of the experimental part in this work. For this reason, the selection of nucleation in this work is primarily aimed at capturing these mechanisms. For the sake of completeness, the third model presented by Boas et al. [52] is also briefly described. The model accounts for coalescence effects of grains containing low-angle grain boundaries, which proves to be a viable approach for lower annealing temperatures (below 0.65 T_m) [49, 53].

References

[1] W. K. Burton, N. Cabrera, F. C. Frank, N. F. Mott, The growth of crystals and the equilibrium structure of their surfaces, Philosophical Transactions of the Royal Society of London. Series A, Mathematical and Physical Sciences 243 (866) (1951) 299–358. doi:10.1098/rsta.1951.0006.
URL https://doi.org/10.1098/rsta.1951.0006

[2] P. Feltham, Grain growth in metals, Acta Metallurgica 5 (2) (1957) 97–105. doi:https://doi.org/10.1016/0001-6160(57)90136-0.
URL https://www.sciencedirect.com/science/article/pii/0001616057901360

[3] P. R. Rios, Abnormal grain growth in materials containing particles, Acta Metallurgica et Materialia 42 (3) (1994) 839–843. doi:https://doi.org/10.1016/0956-7151(94)90278-X.
URL https://www.sciencedirect.com/science/article/pii/095671519490278X

[4] J. E. Burke, D. Turnbull, Recrystallization and grain growth, Progress in Metal Physics 3 (1952) 220–292. doi:https://doi.org/10.1016/0502-8205(52)90009-9.
URL https://www.sciencedirect.com/science/article/pii/0502820552900099

[5] N. P. Louat, On the theory of normal grain growth, Acta Metallurgica 22 (6) (1974) 721–724. doi:https://doi.org/10.1016/0001-6160(74)90081-9.
URL https://www.sciencedirect.com/science/article/pii/0001616074900819

[6] C. E. Krill Iii, L. Q. Chen, Computer simulation of 3-d grain growth using a phase-field model, Acta Materialia 50 (12) (2002) 3059–3075. doi:https://doi.org/10.1016/S1359-6454(02)00084-8.
URL https://www.sciencedirect.com/science/article/pii/S1359645402000848

[7] S. G. Kim, D. I. Kim, W. T. Kim, Y. B. Park, Computer simulations of two-dimensional and three-dimensional ideal grain growth, Physical Review E 74 (6) (2006) 061605. doi:10.1103/PhysRevE.74.061605.
URL https://link.aps.org/doi/10.1103/PhysRevE.74.061605

[8] R. Brandt, W. Graupner, K. Lücke, Normal and abnormal grain growth and particularly the behaviour of large and small grains as predicted by simulations on the basis of the statistical model, in: Grain Growth in Polycrystalline Materials II, Vol. 204 of Materials Science Forum, Trans Tech Publications Ltd, 1996, p. 295–302. doi:10.4028/www.scientific.net/MSF.204-206.295.

[9] M. Winning, A. D. Rollett, G. Gottstein, D. J. Srolovitz, A. Lim, L. S. Shvindlerman, Mobility of low-angle grain boundaries in pure metals, Philosophical Magazine 90 (22) (2010) 3107–3128. doi:10.1080/14786435.2010.481272.
URL https://doi.org/10.1080/14786435.2010.481272

[10] G. H. Zahid, Y. Huang, P. B. Prangnell, Microstructure and texture evolution during annealing a cryogenic-spd processed al-alloy with a nanoscale lamellar hagb grain structure, Acta Materialia 57 (12) (2009) 3509–3521. doi:https://doi.org/10.1016/j.actamat.2009.04.010.
URL https://www.sciencedirect.com/science/article/pii/S135964540900216X

[11] O. V. Mishin, A. Godfrey, D. Juul Jensen, N. Hansen, Recovery and recrystallization in commercial purity aluminum cold rolled to an ultrahigh strain, Acta Materialia 61 (14) (2013) 5354–5364. doi:https://doi.org/10.1016/j.actamat.2013.05.024.
URL http://www.sciencedirect.com/science/article/pii/S1359645413003923

[12] N. Kamikawa, X. Huang, N. Tsuji, N. Hansen, Strengthening mechanisms in nanostructured high-purity aluminium deformed to high strain and annealed, Acta Materialia 57 (14) (2009) 4198–4208. doi:https://doi.org/10.1016/j.actamat.2009.05.017.
URL http://www.sciencedirect.com/science/article/pii/S1359645409003152

[13] C. Y. Yu, P. L. Sun, P. W. Kao, C. P. Chang, Evolution of microstructure during annealing of a severely deformed aluminum, Materials Science and Engineering: A 366 (2) (2004) 310–317. doi:https://doi.org/10.1016/j.msea.2003.08.039.
URL http://www.sciencedirect.com/science/article/pii/S0921509303007457

[14] A. M. Mavlyutov, A. S. Bondarenko, M. Y. Murashkin, E. V. Boltynjuk, R. Z. Valiev, T. S. Orlova, Effect of annealing on microhardness and electrical resistivity of nanostructured spd aluminium, Journal of Alloys and Compounds 698 (2017) 539–546. `doi:https://doi.org/10.1016/j.jallcom.2016.12.240`.
URL `http://www.sciencedirect.com/science/article/pii/S0925838816341664`

[15] F. J. Humphreys, M. Hatherly, Recrystallization and related annealing phenomena, Elsevier, 2012.

[16] P. Rios, Abnormal grain growth development from uniform grain size distributions, Acta Materialia 45 (4) (1997) 1785–1789. `doi:10.1016/S1359-6454(96)00284-4`.
URL `https://www.sciencedirect.com/science/article/pii/S1359645496002844`

[17] A. D. Rollett, A. P. Brahme, C. G. Roberts, An overview of accomplishments and challenges in recrystallization and grain growth, Materials Science Forum 558-559 (2007) 33–42. `doi:10.4028/www.scientific.net/MSF.558-559.33`.
URL `https://www.scientific.net/MSF.558-559.33`

[18] C. Braun, J. M. Dake, C. E. Krill III, R. Birringer, Abnormal grain growth mediated by fractal boundary migration at the nanoscale, Scientific reports 8 (1) (2018) 1592.

[19] B. Nestler, H. Garcke, B. Stinner, Multicomponent alloy solidification: Phase-field modeling and simulations, Physical Review E 71 (4) (2005) 041609. `doi:10.1103/PhysRevE.71.041609`.
URL `https://link.aps.org/doi/10.1103/PhysRevE.71.041609`

[20] Y. Ivanisenko, R. Kulagin, V. Fedorov, A. Mazilkin, T. Scherer, B. Baretzky, H. Hahn, High pressure torsion extrusion as a new severe plastic deformation process, Materials Science and Engineering: A 664 (2016) 247–256. `doi:https://doi.org/10.1016/j.msea.2016.04.008`.
URL `http://www.sciencedirect.com/science/article/pii/S0921509316303719`

[21] R. Kulagin, Y. Beygelzimer, Y. Estrin, Y. Ivanisenko, B. Baretzky, H. Hahn, A mathematical model of deformation under high pressure torsion extrusion, Metals 9 (3) (2019). `doi:10.3390/met9030306`.

[22] N. Brook, The equivalent core diameter method of size and shape correction in point load testing, International Journal of Rock Mechanics and Mining Sciences & Geomechanics Abstracts 22 (2) (1985) 61–70. `doi:10.1016/0148-9062(85)92328-9`.
URL `https://www.sciencedirect.com/science/article/pii/0148906285923289`

[23] M. Calcagnotto, D. Ponge, E. Demir, D. Raabe, Orientation gradients and geometrically necessary dislocations in ultrafine grained dual-phase steels studied by 2d and 3d ebsd, Materials Science and Engineering a-Structural Materials Properties Microstructure and Processing 527 (10-11) (2010) 2738–2746. `doi:10.1016/j.msea.2010.01.004`.
URL `<GotoISI>://WOS:000276137600040`

[24] P. B. Prangnell, J. S. Hayes, J. R. Bowen, P. J. Apps, P. S. Bate, Continuous recrystallisation of lamellar deformation structures produced by severe deformation, Acta Materialia 52 (11) (2004) 3193–3206. `doi:https://doi.org/10.1016/j.actamat.2004.03.019`.
URL `http://www.sciencedirect.com/science/article/pii/S1359645404001661`

[25] D. Chakrabarti, C. Davis, M. Strangwood, Characterisation of bimodal grain structures in hsla steels, Materials Characterization 58 (5) (2007) 423–438. `doi:https://doi.org/10.1016/j.matchar.2006.06.014`.
URL `https://www.sciencedirect.com/science/article/pii/S1044580306002087`

[26] A. Vondrous, P. Bienger, S. Schreijäg, M. Selzer, D. Schneider, B. Nestler, D. Helm, R. Mönig, Combined crystal plasticity and phase-field method for recrystallization in a process chain of sheet metal production, Computational Mechanics 55 (2) (2015) 439–452. `doi:10.1007/s00466-014-1115-0`.
URL `https://doi.org/10.1007/s00466-014-1115-0`

[27] W. T. Read, W. Shockley, Dislocation models of crystal grain boundaries, Physical Review 78 (3) (1950) 275–289. `doi:10.1103/PhysRev.78.275`.
URL `https://link.aps.org/doi/10.1103/PhysRev.78.275`

[28] F. J. Humphreys, A unified theory of recovery, recrystallization and grain growth, based on the stability and growth of cellular microstructures—i. the basic model, Acta Materialia 45 (10) (1997) 4231–4240. `doi:https://doi.org/10.1016/S1359-6454(97)00070-0`.
URL `https://www.sciencedirect.com/science/article/pii/S1359645497000700`

[29] D. Raabe, L. Hantcherli, 2d cellular automaton simulation of the recrystallization texture of an if sheet steel under consideration of zener pinning, Computational Materials Science 34 (4) (2005) 299–313. `doi:https://doi.org/10.1016/j.commatsci.2004.12.067`.
URL `http://www.sciencedirect.com/science/article/pii/S092702560500011X`

[30] J. Hötzer, O. Tschukin, M. B. Said, M. Berghoff, M. Jainta, G. Barthelemy, N. Smorchkov, D. Schneider, M. Selzer, B. Nestler, Calibration of a multi-phase field model with quantitative angle measurement, Journal of materials science 51 (4) (2016) 1788–1797.

[31] I. Steinbach, F. Pezzolla, A generalized field method for multiphase transformations using interface fields, Physica D: Nonlinear Phenomena 134 (4) (1999) 385–393. `doi:https://doi.org/10.1016/S0167-2789(99)00129-3`.
URL `https://www.sciencedirect.com/science/article/pii/S0167278999001293`

[32] I. Steinbach, Phase-field models in materials science, Modelling and simulation in materials science and engineering 17 (7) (2009) 073001.

[33] E. Schoof, Chemomechanische modellierung der wärmebehandlung von stählen mit der phasenfeldmethode, Ph.D. thesis, Karlsruher Institut für Technologie (KIT) (2020). `doi:10.5445/IR/1000117917`.

[34] J. Hötzer, A. Reiter, H. Hierl, P. Steinmetz, M. Selzer, B. Nestler, The parallel multi-physics phase-field framework pace3d, Journal of computational science 26 (2018) 1–12.

[35] A. Vondrous, M. Reichardt, B. Nestler, Growth rate distributions for regular two-dimensional grains with read–shockley grain boundary energy, Modelling and Simulation in Materials Science and Engineering 22 (2) (2014) 025014.

[36] G. Abrivard, E. P. Busso, S. Forest, B. Appolaire, Phase field modelling of grain boundary motion driven by curvature and stored energy gradients. part ii: Application to recrystallisation, Philosophical Magazine 92 (28-30) (2012) 3643–3664. `doi:10.1080/14786435.2012.717726`.
URL `https://doi.org/10.1080/14786435.2012.717726`

[37] G. Abrivard, E. Busso, S. Forest, B. Appolaire, Phase field modelling of grain boundary motion driven by curvature and stored energy gradients. part ii: Application to recrystallisation, Philosophical Magazine 92 (28-30) (2012) 3643–3664. `arXiv:https://doi.org/10.1080/14786435.2012.717726`, `doi:10.1080/14786435.2012.717726`.
URL `https://doi.org/10.1080/14786435.2012.717726`

[38] G. Abrivard, E. P. Busso, S. Forest, B. Appolaire, Phase field modelling of grain boundary motion driven by curvature and stored energy gradients. part i: theory and numerical implementation, Philosophical Magazine 92 (28-30) (2012) 3618–3642. `doi:10.1080/14786435.2012.713135`.
URL `https://doi.org/10.1080/14786435.2012.713135`

[39] V. Yadav, N. Moelans, Y. Zhang, D. Juul Jensen, Influence of geometrical alignment of the deformation microstructure on local migration of grain boundaries during recrystallization: A phase-field study, Scripta Materialia 191 (2021) 116–119. `doi:https://doi.org/10.1016/j.scriptamat.2020.09.028`.
URL `https://www.sciencedirect.com/science/article/pii/S1359646220306278`

[40] Y. Huang, F. Humphreys, Measurements of grain boundary mobility during recrystallization of a single-phase aluminium alloy, Acta Materialia 47 (7) (1999) 2259–2268.

[41] M. L. Taheri, D. Molodov, G. Gottstein, A. D. Rollett, Grain boundary mobility under a stored-energy driving force: a comparison to curvature-driven boundary migration, Zeitschrift für Metallkunde

96 (10) (2005) 1166–1170. doi:10.3139/146.101157.
URL https://doi.org/10.3139/146.101157

[42] W. Rheinheimer, E. Schoof, M. Selzer, B. Nestler, M. J. Hoffmann, Non-arrhenius grain growth in strontium titanate: Quantification of bimodal grain growth, Acta Materialia 174 (2019) 105–115. doi:https://doi.org/10.1016/j.actamat.2019.05.040.
URL http://www.sciencedirect.com/science/article/pii/S1359645419303246

[43] P. R. Rios, F. Siciliano Jr, H. R. Z. Sandim, R. L. Plaut, A. F. Padilha, Nucleation and growth during recrystallization, Materials Research 8 (3) (2005) 225–238.

[44] R. D. Doherty, D. A. Hughes, F. J. Humphreys, J. J. Jonas, D. J. Jensen, M. E. Kassner, W. E. King, T. R. McNelley, H. J. McQueen, A. D. Rollett, Current issues in recrystallization: a review, Materials Science and Engineering: A 238 (2) (1997) 219–274. doi:https://doi.org/10.1016/S0921-5093(97)00424-3.
URL https://www.sciencedirect.com/science/article/pii/S0921509397004243

[45] P. A. Beck, P. R. Sperry, Strain induced grain boundary migration in high purity aluminum, Journal of Applied Physics 21 (2) (1950) 150–152. doi:10.1063/1.1699614.
URL https://doi.org/10.1063/1.1699614

[46] A. H. Cottrell, Theory of dislocations, Progress in Metal Physics 4 (1953) 205–264.

[47] P. A. Beck, The formation of recrystallization nuclei, Journal of Applied Physics 20 (6) (1949) 633–634.

[48] R. W. Cahn, A new theory of recrystallization nuclei, Proceedings of the Physical Society. Section A 63 (4) (1950) 323. doi:10.1088/0370-1298/63/4/302.
URL https://dx.doi.org/10.1088/0370-1298/63/4/302

[49] R. Sandström, B. Lehtinen, E. Hedman, I. Groza, S. Karlsson, Subgrain growth in al and al-1% mn during annealing, Journal of Materials Science 13 (6) (1978) 1229–1242. doi:10.1007/BF00544729.
URL https://doi.org/10.1007/BF00544729

[50] S. Varma, B. L. Willits, Subgrain growth in aluminum during static annealing, Metallurgical Transactions A 15 (7) (1984) 1502–1503.

[51] W. Blum, C. Schlögl, M. Meier, Subgrain formation and subgrain boundary migration in al-5mg during high temperature deformation in the range of class a behaviour in comparison with pure aluminium, International Journal of Materials Research 86 (9) (1995) 631–637. doi:doi:10.1515/ijmr-1995-860909.
URL https://doi.org/10.1515/ijmr-1995-860909

[52] W. Boas, J. Bowles, The effect of crystal arrangement on" secondary recrystallization" in metals, J INST MET 74 (1947) 501–519.

[53] R. D. Doherty, J. A. Szpunar, Kinetics of sub-grain coalescence—a reconsideration of the theory, Acta Metallurgica 32 (10) (1984) 1789–1798. doi:https://doi.org/10.1016/0001-6160(84)90235-9.
URL https://www.sciencedirect.com/science/article/pii/0001616084902359